Population receptive fields of human primary visual cortex organised as DC-balanced bandpass filters.

Daniel Gramm Kristensen[1] & Kristian Sandberg[1]

[1]Department of Clinical Medicine, Center of Functionally Integrative Neuroscience, Aarhus University, Denmark.

Corresponding author:
Daniel Gramm Kristensen
Center of Functionally Integrative Neuroscience
Aarhus University Hospital Nørrebrogade 44
Building 1A 8000 Aarhus C Denmark
Email: dgramm@cfin.au.dk

Abstract

Visual receptive fields are characterised by their centre-surround organisation and are typically modelled by Difference-of-Gaussians (DoGs). The DoG captures the effect of surround modulation, where the central receptive field can be modulated by simultaneous stimulation of a surrounding area. Although it is well-established that this centre-surround organisation is crucial for extracting spatial information from visual scenes, the principles guiding this information processing are unclear. Here, we present an organisational principle that describes how the receptive field centre and surround can be balanced to achieve DC-balanced signal processing, which optimises the bandpass properties of the DoG model. Using computational modelling of human fMRI data, we demonstrate that population Receptive Fields (pRF) in primary visual cortex (V1) adhere to this principle. We infer that surround modulation is the likely mechanism responsible for the balancing, and we speculate on how the physiological structure of neurons and their interconnections provide a highly plausible framework of implementation for the proposed mechanism. Finally, we explore how the uncertainty principle for information sheds light on the advantageousness of the receptive field configuration principle for biological information processing.

Introduction

Visual receptive fields are characterised by their centre-surround organisation. The mechanism of surround modulation was first described when it was discovered that simultaneous stimulation of two neighboring ommatidia elicited a weaker response compared to stimulation of a single ommatidium (Hartline, Wagner, & Ratliff, 1956), thus revealing a form of surround modulation, namely surround suppression. Since then, it has been found that surround modulation is present in many species (Blakemore & Tobin, 1972; Cavanaugh, Bair, & Movshon, 2002; den Bergh, Zhang, Arckens, & Chino, 2010; Nelson & Frost, 1978; Sceniak, Hawken, & Shapley, 2001; Shushruth, Ichida, Levitt, & Angelucci, 2009) and several sensory modalities (Olsen & Wilson, 2008; Sachdev, Krause, & Mazer, 2012; Sutter, Schreiner, McLean, O'Connor, & Loftus, 1999; Vega & Johnson, 1999), is pervasive throughout the visual system (Albright & Stoner, 2002; Allman, Miezin, & McGuinness, 1985), and that it may also be facilitative (Shushruth et al., 2012; Slllito, Grieve, Jones, Cudeiro, & Davls, 1995). Surround modulation is therefore believed to be key in our understanding of how biological systems process information, yet its precise functional role is unclear (Nurminen & Angelucci, 2014). Here, we present a principle for the organisation of receptive fields that effectively allows it to function as a biologically ideal bandpass filter, thus enabling optimal processing of incoming information. We further use computational modelling of human fMRI data to demonstrate that population receptive fields adhere to the principle, and we demonstrate how this enables the receptive fields to adapt to local contrast such that areas of the visual scene with different mean intensity are normalised, which enables the spatial frequency spectrum to be sampled and compared on the same baseline.

The principle is founded in the characteristics of neuronal receptive fields. A visual receptive field is typically modelled with Difference of Gaussians (DoG) (Rodieck, 1965) that consists of a small central, positive Gaussian surrounded by a larger, negative Gaussian.

$$f(x,y) = e^{\frac{-(x^2+y^2)}{2\sigma_1^2}} - \delta e^{\frac{-(x^2+y^2)}{2\sigma_2^2}} \tag{1}$$

where x and y is the 2D spatial position of the model, σ_1 and σ_2 are the standard deviations of the two Gaussians and δ is a parameter that modulates the amplitude of the second negative Gaussian. The size ratio of these two Gaussians is here parameterised by the standard deviations of the negative, larger Gaussian (σ_2) divided by the positive, smaller Gaussian (σ_1). See Methods for specifics on the model employed here.

The DoG acts as a bandpass filter (Kovesi, 2010), and in the analysis of signals using filters, it is of particular interest how the filter treats the Direct-Current (DC) component of the signal as this influences – for example – how the filter treats signals with the same spatial frequency and amplitude, but different absolute intensity. Filters that blocks or omits the DC-component of the signal are known as DC-balanced filters. There are many ways of characterising the DC-component of a signal, but in most cases, the DC-component refers to the average value over some interval. The choice of interval (i.e. filter window size) may have great impact on the result, but since we are here mainly concerned with Gaussian filters, the choice of filter window size has been made so that the normally infinite Gaussian reaches at least 10^{-6} before cut-off to ensure that the window size has minimum impact on the filtering operation. In many signal processing techniques, the DC-component is often removed, as it is said that information contained therein is redundant (Hyvärinen, Hurri, & Hoyer, 2009) or irrelevant depending on the desired outcome (Gonzalez & Woods, 2002). However, in the following we argue that the DC-balanced DoG filter also holds the advantage of local contrast normalisation, which allows the filter to compare signals of any mean intensity to one another or, alternatively, a group of filters to process a set of signals using the same baseline. Furthermore, we argue that a functional role for surround modulation may be to vary the spatial extent of the DoG filter's constituent parts to achieve DC-balance. This also allows the visual system to select specific features of the visual scene dependent on lighting conditions and the goal of the visual process.

To demonstrate the DC-component of a signal, Figure 1A and 1B illustrates how the DC-component can be identified using an averaging filter. Figure 1A shows three sinusoidal signals. In light grey, a signal of 0.05 cycles per unit distance (c/d), in grey a signal of 0.1 c/d, and finally in black a signal of 0.025 c/d. In Figure 1B, an averaging filter is applied at every entry of the signal vector from left to right. Here, the choice of window size greatly influences the outcome, but for simplicity, a window size of 41 has been chosen so that the outcome is linear. For a given entry in the signal vector, in addition to the entry itself, the filter sums the 20 nearest neighbours to the left of the entry and the 20 nearest neighbours to the right of the entry and multiplies the result with 1/(window size), which is what the inset in blue illustrates (not to scale). The three lines in Figure 1B are the resulting DC-components for the respective signals in Figure 1A. Since there are no entries for the 20 leftmost neighbours for the first 20 iterations of the filter operation, this particular implementation of the averaging filter assumes that these values are zero. This is why the filtered signals in Figure 1B starts at zero and reaches a steady state after a few iterations. To remove the DC-component of the signals in Figure 1A, the result in Figure 1B is subtracted from the original signals. Note, however, that the averaging filter cannot represent the frequency information of the signals.

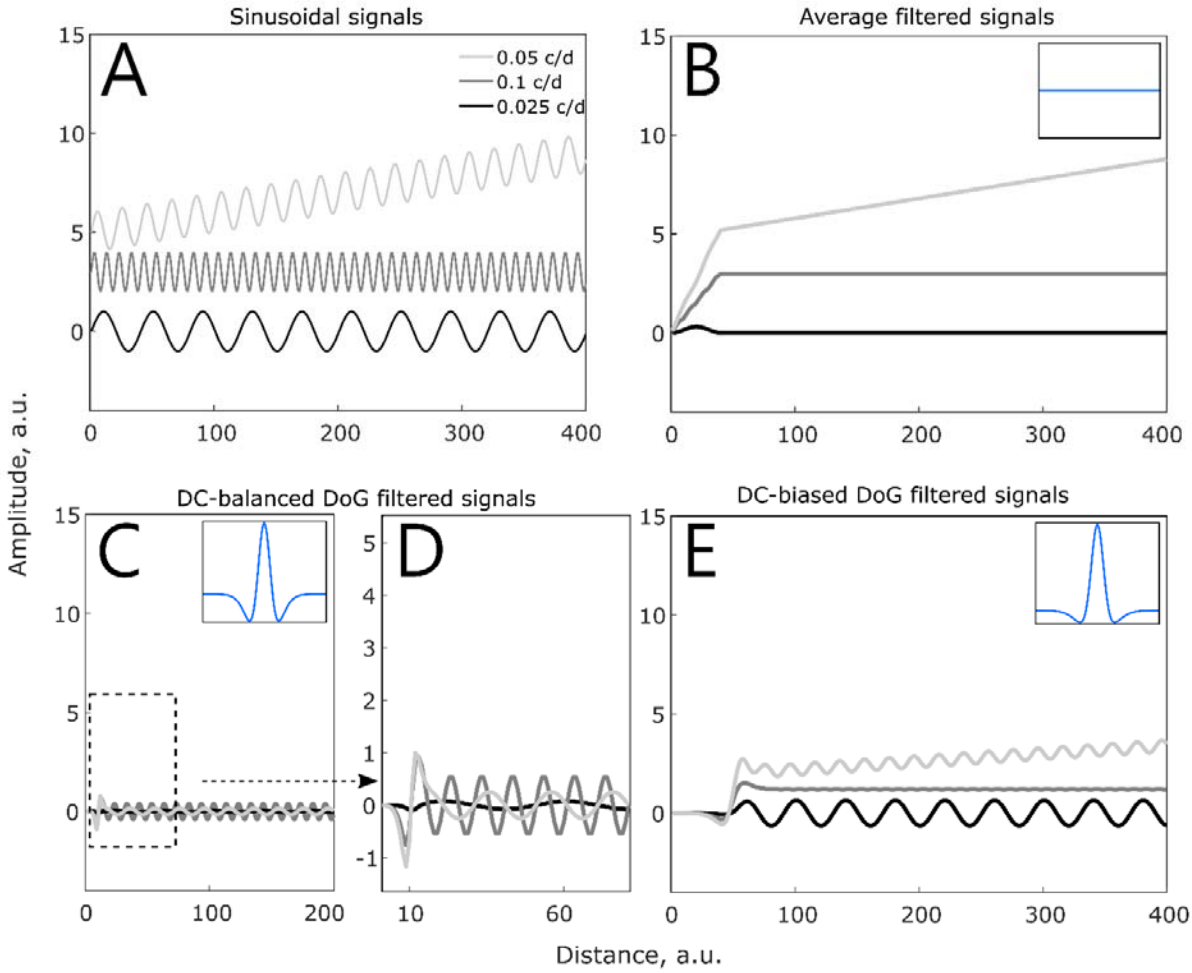

Figure 1. DC-component characteristics. A: Two DC-biased signals and one DC-balanced sinusoidal signal in the spatial domain. **B:** DC-component of the signals in A computed with an averaging filter (inset). **C:** Signals in A filtered with a DC-balanced DoG filter (inset). **D:** Same as C, but magnified. **E:** Signals in A filtered with a DC-biased DoG filter (inset).

Figure 1C and 1D demonstrates the same process, but with a DC-balanced DoG filter. Because this filter is DC-balanced, it is immediately evident that the DC-component of the signals is filtered out, although the amplitude of the signals has also been impacted. The low frequencies have suffered more, and the cause of this is the specific bandpass properties of the DoG filter, which makes the filter more sensitive to some frequencies than to others. We will return to this aspect of the DoG filter later. What is of particular interest here is what happens to the signal when filtered with a DC-biased DoG. This is shown in Figure 1E. Here, it can be observed that there is the same frequency-amplitude dependence, but that the DC-component is only removed from the the signal where there was none to begin with. What this roughly demonstrates is that the DC-balanced DoG filter removes the DC-component of any signal while maintaining the signals' frequency and (to some extent) amplitude characteristics, whereas the DC-biased DoG does not.

We will now attempt to establish how to determine whether a given DoG is DC-balanced or not. Due to the retinotopic organization of the visual system, signals with two spatial dimensions are investigated. Taking

this into account, we reason that the DoG is DC-balanced when the double integral of the 2D spatial filter equals zero, such that

$$\iint_{-\infty}^{\infty} e^{\frac{-(x-x0)^2+(y-yo)^2}{2\sigma_1^2}} - \delta e^{\frac{-(x-x0)^2+(y-yo)^2}{2\sigma_2^2}} = 0 \qquad (2)$$

By this rationale, it is possible to calculate which combination of σ_1, σ_2 and δ that results in a DC-balanced filter as long as two of the variables are known. For example, for any given combination of σ_1 and σ_2, a δ can be calculated that achieves a DC-balanced filter. Figure 2A and 2B illustrates this for a size ($\sigma_{2/}$ σ_1) ratio of $\sqrt{2}$. Here, it can be seen that there is no DC-component only when $\delta = 0.5$ as this is the only δ for which there is no peak in the frequency domain at 0 cycles per degree visual angle in Figure 2B. The three bandpass parameters (peak frequency, bandwidth and amplitude) are further shown specifically for the DoG with $\delta = 0.5$ in Figure 2B. Figure 2C shows the results of similar calculations in the spatial domain with a σ_1 of 1.1 with a range of combinations of size and gain ratios resulting in DC-balanced filters as shown by the corresponding representation in the frequency domain in Figure 2D. Figure 2E and 2F are similar to 2C and 2D, but with a σ_1 value of 2.5. Notice that the size and gain ratios are the same in 2C-D and 2E-F, but the response profile differs significantly, thus creating filters with e.g. different peak frequencies. This is because the specific σ values to achieve these size ratios are not the same. This illustrates that a particular arrangement of the size and gain ratio is crucial in achieving DC-balanced filtering and thus in selecting a particular range of frequencies. It also shows that the arrangement is independent of the specific frequencies the filters select, which is closer tied to the overall size of the filter. The relationship between the filter's size in the spatial domain and its frequency representation will be discussed later. In light of the above demonstration of the importance of DC-balanced filters, we investigate whether or not biological receptive fields are DC-balanced using equation 2.

This was done by measuring surround modulation with fMRI using population Receptive Field (pRF) mapping in conjunction with a DoG receptive field model. In order to test if evidence for DC-balanced filtering can be found in human observers, we mapped the pRFs in a sample of 22 healthy human participants. Participants were placed in the bore of a Siemens Magnotom 3T Skyra. Through a mirror, they were presented with expanding/contracting rings simultaneously with clockwise/counter-clockwise rotating wedges with high-contrast ripple-like textures (Schwarzkopf, Anderson, de Haas, White, & Rees, 2014). We also acquired high-resolution T1 structural images for each participant and used these for an anatomical reconstruction in Freesurfer. A delineation of each participant's primary visual cortex (V1) was made from a prediction using landmarks from this anatomical reconstruction using a built-in Freesurfer algorithm (Hinds et al., 2008). From these images, we were able to obtain the σ and δ parameters for voxels within each participant's V1.

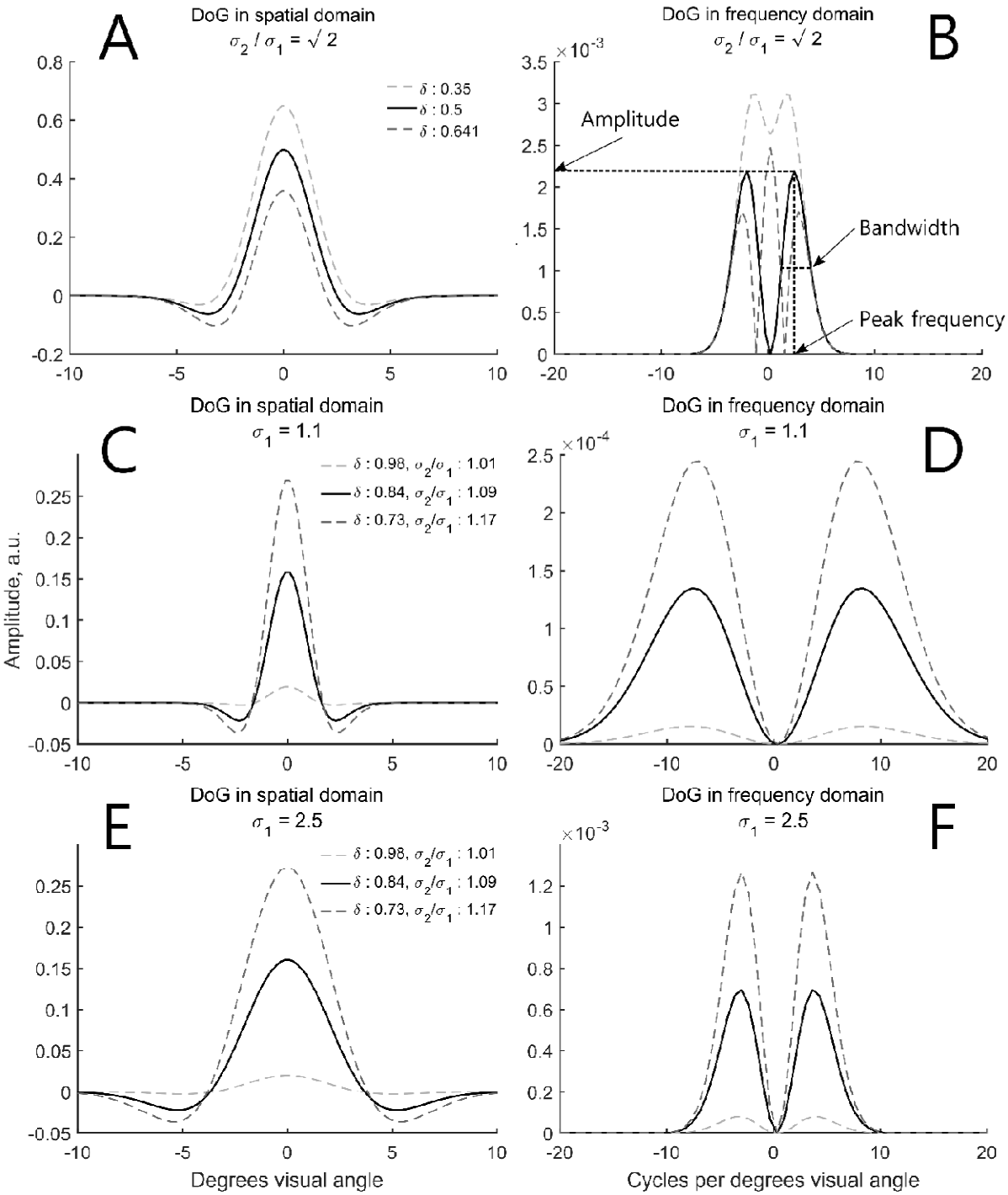

Figure 2. Size (σ_2/σ_1) and gain ratios (δ) for simulated DoG models. **A** (spatial domain) and **B** (frequency domain) show that a DoG with a size ratio ¯ is DC-balanced when the gain ratio is 0.5, which is not the case for any of the other δ values as evidenced by the large peak around 0 in the frequency domain. **C** and **D** show that for any given size ratio, there is a corresponding gain ratio that is DC-balanced for filters with a σ_1 of.6. **E and F** have the same size and gain ratio as C and D, but with a σ_1 of 2.5. For all panels, legends in the spatial domain (left) also apply in the frequency domain (right).

Results

For each participant, a pRF profile was created for each of 17 eccentricity bins of 1 degree visual angle (dva) for each hemisphere (0.5 – 17.5 dva). For each of these pRF profiles, we first estimated the σ_1, σ_2 and δ, and then used σ_1 and δ to compute the σ_2 that would yield a DC-balanced filter (in accord with equation 2). Figure 3A shows the logarithmically transformed observed σ_2 plotted against the computed σ_2 (see Online Methods and SI Fig. 1 for examples of this calculation for individual participants without bins). From these two datasets, we then calculated their bandpass parameters (peak frequency, amplitude and bandwidth). Figure 3B-D shows the computed bandpass parameters plotted against the observed bandpass parameters after logarithmic transformation. The bandpass parameters are entirely dependent on the spatial pRF profile. The reason for reporting them separately should become clear in the following sections.

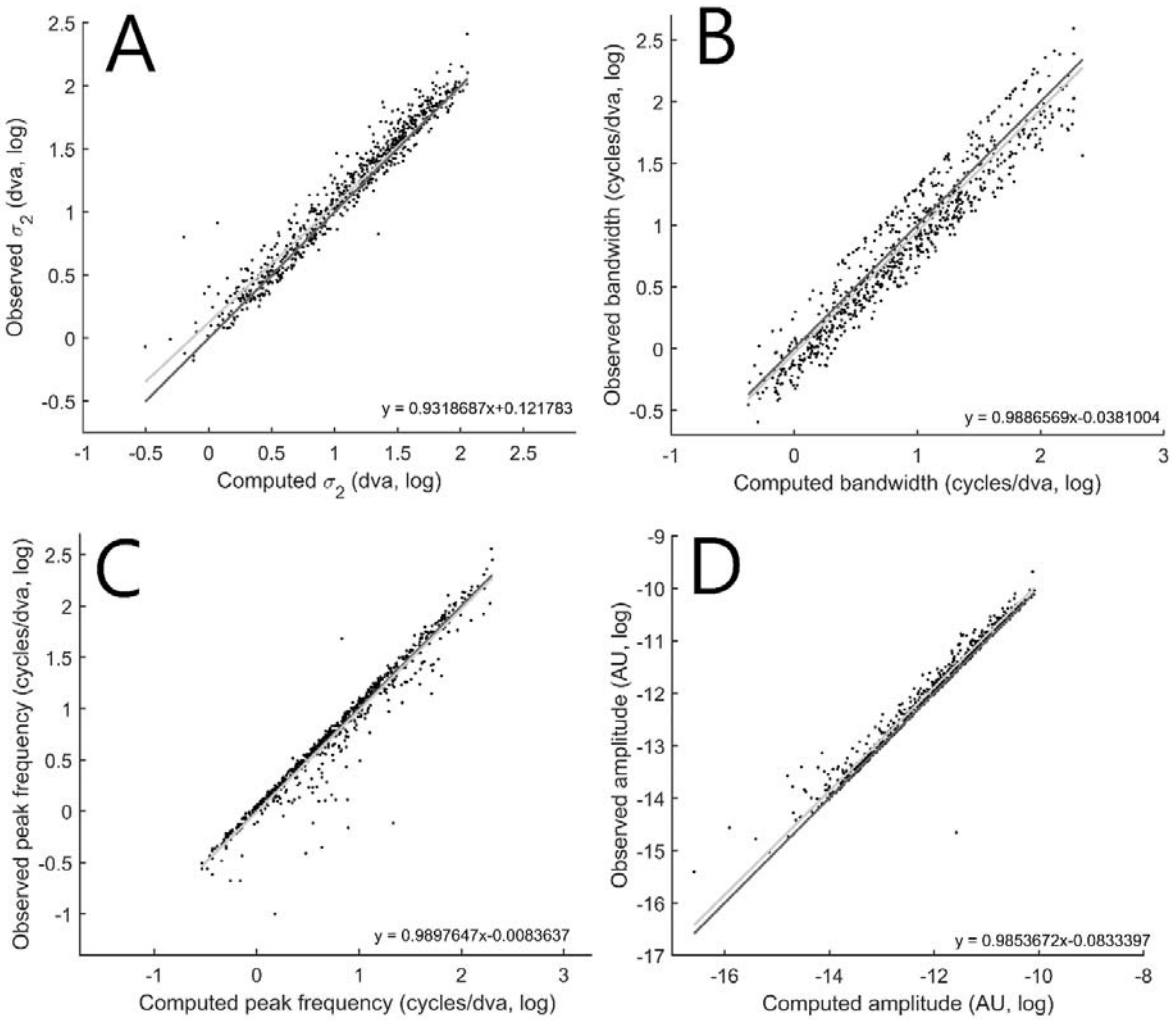

Figure 3. Observed and computed DoG parameters. A: observed σ_2 plotted against the computed σ_2. **B**, **C**, & **D:** observed compared with the computed bandpass parameters. Correlation line is plotted in dark grey, identity line is plotted in light grey.

To compare the observed with the computed pRF profile parameters, we used random coefficient models for each parameter separately, providing the linear fits shown in Figure 3A-D (dark grey). The results were

highly significant for all parameters: σ_2 (Wald $\chi^2(1) = 1347.26$, $p < 0.00001$, slope 95% CI: 0.8821 to 0.9816, intercept 95% CI: 0.0652 to 0.1783), bandwidth (Wald $\chi^2(1) = 1403.12$, $p < 0.00001$, slope 95% CI: 0.9369 to 1.0403, intercept 95% CI: -0. 0854 to 0.0092), peak frequency (Wald $\chi^2(1) = 5621.18$, $p < 0.00001$, slope 95% CI: 0.9639 to 1.0156, intercept 95% CI: -0.0327 to 0.0160), and amplitude (Wald $\chi^2(1) = 9048.87$, $p < 0.00001$, slope 95% CI: 0.9651 to 1.0057, intercept 95% CI: -0.3308 to 0.1642). Note that for all parameters, the linear model has a near-one slope and a near-zero intercept which places the regression line close to the identity line (light grey). These findings suggest that the modelled DoG pRF profiles of our participants are close to being DC-balanced.

To develop a deeper understanding of why DC-balanced filters are important for processing certain visual information, it is useful to examine the relationship between the space and frequency domains through the uncertainty principle (Heisenberg, 1927; Kennard, 1927). In Gabor's seminal 1946 paper '*Theory of Communication'* (Gabor, 1946), he derived the uncertainty principle for information based on Heisenberg's earlier discovery in quantum physics. Here, Gabor outlines the general family of filters that optimize the trade-off between the joint uncertainty of signals in the time and frequency domains. Daugman later developed this theory for two-dimensional spatial filters using the same filter family, now known as Gabor filters. Daugman showed that these types of spatial filters are limited in their attainable information resolution for spatial frequency, orientation, and location (Daugman, 1985). Gabor functions, however, are complex-valued functions and it was argued that they are difficult to envision in a biological system (Stork & Wilson, 1990). Instead, a family of real-valued functions that optimises the same uncertainty relation was proposed, namely Gaussians and derivatives thereof, where the DoG approximates the second derivative of a Gaussian (Lindeberg, 2013; Marr & Hildreth, 1980).

This gives two facets of the uncertainty principle for information. The first is a consequence of the quantum nature of reality and is what sets the lower limit for the joint uncertainty of two complementary variables. This is of little importance on the scale we are dealing with here. The second facet, however, states that for a given sampling rate, a decrease in the uncertainty in one domain will increase the uncertainty in the other domain. The two complementary variables we are investigating here, is spatial position and spatial frequency. The uncertainty principle for information is typically defined with Gaussian distributions, and it is custom to express the degree of uncertainty in terms of Gaussian standard deviations. Here, we examine the uncertainty principle in relation to the DoG and express the degree of uncertainty as the full width at half maximum for convenience.

Figure 4A shows the log-transformed FWHM in the frequency and the spatial domain for the observed σ_1 (black circles) as well as the observed (black dots) and computed DoG (grey dots). Figure 4B shows the log-transformed FWHM in the frequency and the spatial domain for the observed σ_2 (black crosses) as well as the observed (black dots) and computed DoG (grey dots). The anti-symmetry between the two domains that the uncertainty principle commands is confirmed by the negative relationship between all parameters; as certainty is increased in one domain, it is lowered correspondingly in the other domain.

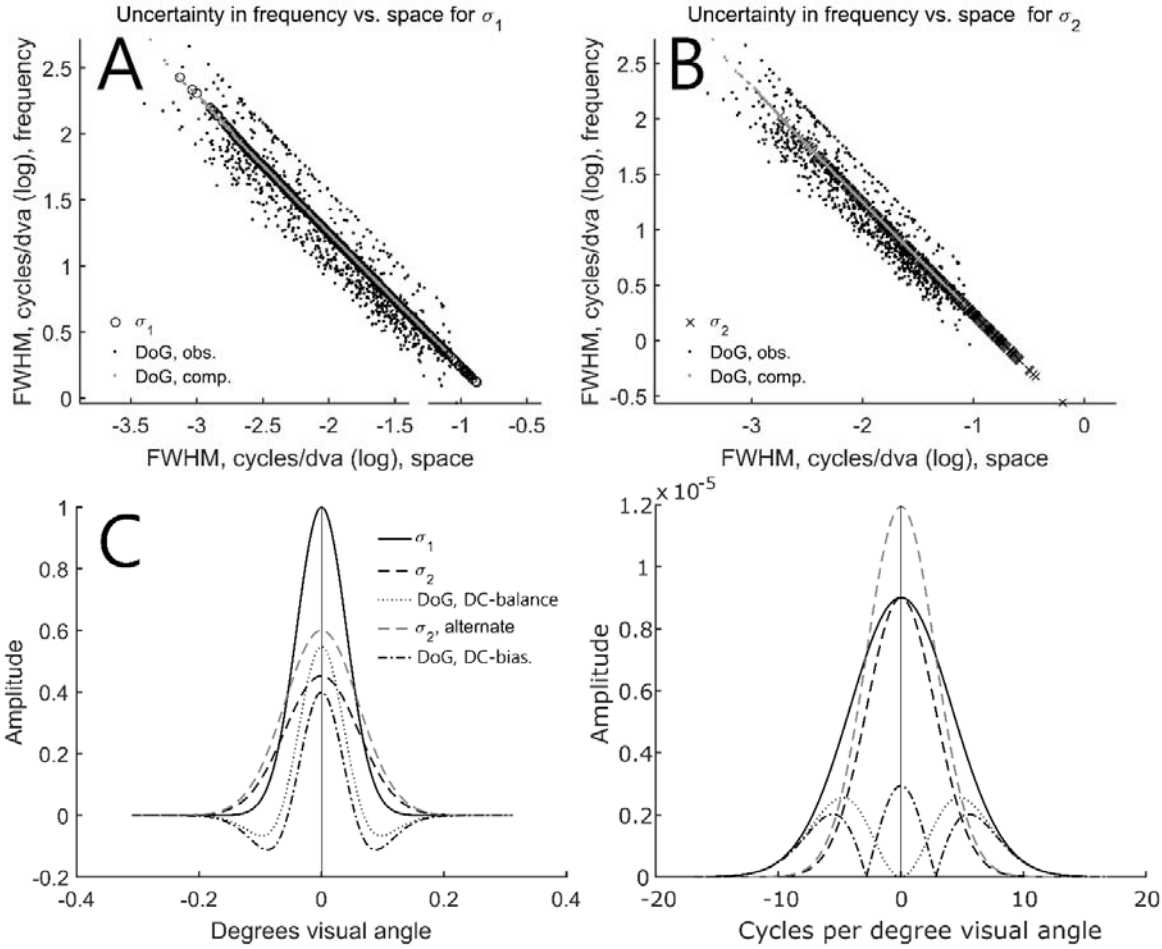

Figure 4. Uncertainty in space and spatial frequency. A: Bandwidth in FWHM of the two Gaussians, σ1 and σ2, composing the DoG as well as the bandwidth in FWHM of the observed and computed DoG filters plotted in the spatial and the frequency domain. **B**: Bandwidth compared with peak frequency for the observed and computed DoG filters. **C**: Cross-sections of the individual parts of the 2D DoG and the combined DoG for both a DC-balanced and a DC-biased filter plotted in the spatial domain. **D**: Same as C, but plotted in the frequency domain.

Figure 4C-D illustrates examples of this inverse relationship. These plots are cross-sections of the filter profile of single points in Figure 4A and 4B - except the alternate σ_2 (grey dashed line) which has been left out of Figure 4A and 4B for simplicity. We have included the alternate σ_2 in Figure 4C and D to illustrate how this parameter in combination with σ_1 gives a DC-offset filter (dash-dotted line). The value of the alternate σ_2 is the same as σ_2 multiplied by a small constant chosen to be 0.6 in this case (for plotting purposes). Initially, one could be led to believe that the DC-offset DoG disobeys the uncertainty principle by being able to occupy points lower than the main diagonal of Figure 4A, but this is only because the large DC-component in the frequency domain is not taken into account when calculating the FWHM (the peak of the black dash-dotted curve centred at 0 in Figure 4D).

A system processing visual information using only Gaussians could, in theory, capture high spatial frequencies to some degree. However, due to the anti-symmetry of the uncertainty principle, such an approach quickly leads to ever-smaller filters in the spatial domain, which, in turn, increases the uncertainty in the frequency domain. The DC-balanced DoG filter circumvents this paradox by processing the same

information twice. Taking the difference of two Gaussians, slightly different in size, allows the DoG filter to redistribute much of the low-frequency bandwidth towards the higher frequencies. This gives a greater degree of certainty for the higher frequencies and will be most efficient if the DoG filter is DC-balanced. This is because a large DC-component would unnecessarily allocate a large portion of the available bandwidth to the lowest frequencies while simultaneously eliminating the filter's ability to select a narrow continuous band of frequencies.

Note that the limitations imposed by the uncertainty principle of information are never surpassed by DoG filtering. By allowing a slight temporal delay due to the extra computations required to process the same information twice, the limitations of the uncertainty principle can be relaxed (not shown here). This also hints at a, to our knowledge, yet to be defined extension of the uncertainty principle for information where the temporal domain enters alongside the trade-off between certainty in the spatial and the spatial frequency domains. In this way, the bandwidth can be distributed amongst the various domains according to the demands of a particular visual task.

Discussion

DC-balanced DoG filtering allows for allocation of bandwidth from potentially redundant frequencies to specific frequencies of interest. Here, we examined the role of DC-balanced filtering in biological perception by first highlighting that DC-balanced filtering is achieved when the double integral of the DoG receptive field model equals zero. Next, we modelled receptive fields for populations of human V1 neurons using fMRI, and we found that the DoG parameters obtained from fitting the model to the experimental data yielded highly similar parameters to those of a DC-balanced model, thus providing evidence for DC-balanced filtering in human V1. The results reveal how an organisational principle enables the visual system to adapt its sampling strategy to optimally cover the stimulus-space relevant to the organism in a manner that we argue is restricted by the uncertainty principle for information.

There are several advantages of the DC-balanced DoG filter. The DC-balanced DoG filter is particularly suited for picking out object boundaries because these are characterised by higher spatial frequencies (the sharper the boundary, the higher the frequency) and the DC-balanced DoG filter is better able to isolate these higher frequencies for separate processing compared to the DC-biased DoG. Furthermore, since the DC-component is thought to be redundant, its removal can be said to increase efficiency of the neural coding (Barlow, 1961; Field, 1987), and the DC-balanced DoG achieves this while the DC-biased DoG does not. Removing the DC-component is also a form of local contrast normalisation (or adaptation), which has been shown to increase performance of object feature extraction (Dalal & Triggs, 2005). Finally, since the visual signal can vary several orders of magnitude in the same visual scene, removing the DC-component of the signal allows frequencies of otherwise different mean intensity to be compared on equal footing, so to speak.

Taken together, we speculate that surround modulation acts as a mediator between the complementary variables of the uncertainty principle of information according to stimulus conditions and goal of the specific visual process. This mediation can be said to be optimal when the relative strength and spatial extent of the centre and surround results in a DC-balanced bandpass filter that selects the spatial frequencies of interest with sufficiently high certainty for the task. The physiological structure and function of neurons and their interconnections provide a highly plausible framework of implementation for the proposed mechanism of DC-balanced filtering. Structurally, the maximum receptive field size of a neuron's classical and extra-classical receptive field (i.e. $\sigma 1$ and $\sigma 2$) will depend on the dendritic branching of the neuron and the neurons to which it is connected. The functionally defined receptive field size depends on the specific computations

that are being carried out. The structurally defined receptive field and the functionally defined receptive field may therefore not be the same. For example, information from neighbouring neurons can be inhibited resulting in a decrease in the functionally defined extra-classical receptive field ($\sigma 2$), which, as we have shown, changes what spatial frequencies the neuron is most sensitive to, while the structurally defined receptive field remains the same. Similarly, the magnitude of interneuronal influence will depend on the physiological structure of the neuron's dendrites as well as its synapses and the functional release of neurotransmitters, and these aspects will in turn influence the amplitude parameter in our presented equation. Together, this provides a biologically plausible frame of implementation of the computations implied in our presented equation.

In other words, DC-balanced filtering could thus be viewed not simply as an analogue or a new way of thinking about brain computations, but something that arises as a natural consequence of brain organisation and function, or perhaps rather, that the brain through learning structurally arrives at an organisation able to compute a range of the most relevant spatial frequencies for a given area of the visual field, while functionally possessing the ability to adapt to the specific visual scene. While we present a biologically plausible framework for the implementation of DC-balanced filtering, it must be acknowledged that fMRI does not immediately provide the opportunity to validate the specific cellular and subcellular aspects, and the method consequently does not allow us to validate the occurrence of the proposed receptive field organisation at the single neuron level. Follow-up animal studies could nevertheless address these limitations.

Apart from what has already been discussed, there are some further limitations to the study presented here. Firstly, the pRF model-fitting procedure uses a Nelder-Mead search algorithm to find the global minimum in a 6-dimensional parameter-space where the initial starting point is selected by taking the highest correlation between the observed signal and a coarse representation of the parameter space. This approach can cause the Nelder-Mead search to be caught in a local minimum and therefore fail to find the best fitting parameter set. However, most of such failed fits will show poor correlation with the observed data and are therefore removed from the dataset due to the minimum 5% BOLD variance explained criterion. See Methods for details. It is possible that some failed fits are still included in the dataset, but they should only introduce random noise or some of the occasional outliers in the dataset as it is highly unlikely that the failed fits are numerous enough and occur in a systematic manner that would result in false correlations.

Second, as discussed by Zuiderbaan et al. (Zuiderbaan, Harvey, & Dumoulin, 2012), at higher eccentricities, neuronal position scatter might cause an increase in pRF size despite unchanged neuronal RF sizes. Our estimates for DC-balance at higher eccentricities are therefore likely not as accurate as those at lower eccentricities. This could introduce added noise at lower frequencies (as higher eccentricities have larger receptive fields), potentially increasing heteroscedasticity in analyses involving e.g. peak frequency. In practice, however, heteroscedasticity appears minimal and to not have influenced analysis, and the influence of the potential confound is thus likely negligible. Finally, because of the way we compute the bandpass parameters, there are certain cases where the observed value will correspond to the computed value despite the observed filter having a markedly different profile. An example of this is given in SI Figure 2A for peak frequency. In other cases, because of how the DC-bias affects the filter profile in the frequency domain, especially the bandwidth will become difficult to compare between the two filter states without further parameterization, as is illustrated in SI Figure 2A-D. Since these cases are difficult to identify algorithmically, we have visually inspected a large number of these plots and found that these false correlations are rare and therefore cannot explain the correlation between the observed and computed

bandpass parameters. It is important to note that these caveats only apply to the bandpass parameters and not the correlation for observed versus computed σ_2 (Figure 3A).

In conclusion, we believe to have demonstrated the requirements for a typical DoG model to be DC-balanced and have shown that the pRF profiles of human primary visual cortex gravitate towards DC-balance. We argue that the DC-balanced DoG filter is superior to the DC-biased DoG in its theorised functions, and we argue that the physiological structure of neurons and their interconnections provide a highly plausible framework of implementation of DC-balanced DoG filters. We further hope to have made clear the benefits of including the uncertainty principle for information in the goal of understanding the functional organisation of the receptive fields of the visual system, and how this organisation affects the capabilities of the visual system to process visual information. Finally, we speculate that surround modulation may be the mechanism that mediates these aspects of visual information processing.

Methods

Participants

This study was approved by the local ethics committee, De Videnskabsetiske Komitéer for Region Midtjylland, and conducted according to the principles of the Declaration of Helsinki. 24 healthy, right-handed adults with normal or corrected-to-normal visual acuity aged between 18 and 40 (14 females) gave informed consent to participate in the study. 2 participants were excluded because we failed to generate a meaningful pRF map for either one or both hemispheres.

MRI and stimuli

The stimuli were similar to those used in conventional retinotopic mapping (Sereno et al., 1995) and consisted of expanding/contracting rings and clockwise/counterclockwise rotating wedges with a high-contrast ripple-like texture and mean luminance of 87 cd/m^2. The stimuli subtended a maximum of 17.4° visual angle.

Procedure

Participants were placed in the bore of a Siemens Magnetom Skyra 3T MRI scanner. Stimuli were projected onto a screen in the back of the scanner and viewed by the participant through a mirror placed on top of the head coil. Participants were instructed to maintain fixation on a small black dot in the centre of the screen and at pseudo-random intervals, the dot would change colour to red. To control eye-fixation and overt attention, participants were instructed to press a button when this occurred.

Stimulus presentation and recording of behavioural responses was implemented using the Psychophysics Toolbox 3 (Brainard, 1997; Pelli, 1997) running under MATLAB 2013a. Population Receptive Field mapping was implemented using custom scripts. fMRI images were acquired using a 32-channel head coil with the top removed (for better participant view) resulting in 20 remaining channels.

176 whole-brain volumes of high-resolution structural images were acquired using a T1-weighted coronal-oriented MP2RAGE sequence (TR: 5000ms, TE: 2.98ms; field of view: 240 x 256 x 176mm, voxel size: 1mm^3 isotropic) using a 32-channel head coil.

The pRF mapping protocol acquired 15 continuous axial slices (slice-thickness: 2mm) for each volume using a T2*-sensitive gradient echoplanar Imaging (EPI) sequence (TR: 1000 ms; TE: 30 ms; flip angle: 60°; field

of view: 192 x 192 x 30 mm; voxel size: 2x2x2 mm, GRAPPA with PAT-factor 2). 6 runs of 225 volumes were acquired for each participant (3 clockwise and 3 counter-clockwise).

MRI analysis

Image preprocessing was carried out using Statistical Parametric Mapping (SPM12; Wellcome Department of Imaging Neuroscience, London, UK) running under MATLAB R2013a. For each participant, volumes from the pRF mapping were realigned to the first image of the run to correct for head motion, unwarped using a presubstracted phase and magnitude B_0 field map to correct for geometric distortions, and slice-time corrected for acquisition delays. Next, the first image of the first run was coregistered to the high-resolution structural and subsequently these coregistration parameters were applied to all other images from the remaining runs. The structural images were used for cortical reconstruction and volumetric segmentation within the Freesurfer image analysis suite (Dale, Fischl, & Sereno, 1999; Fischl, Sereno, & Dale, 1999) to create an inflated 3D image of the grey/white-matter boundary for each participant. Based on this reconstruction, a prediction of the anatomical extent of V1 was created using a built-in Freesurfer algorithm (Hinds et al., 2008). This V1 delineation was used as a mask for constraining which voxels to include in the following pRF analysis.

pRF analysis

A full account of the pRF analysis procedure has been given by Dumoulin and Wandell (Dumoulin & Wandell, 2008; Harvey & Dumoulin, 2012). In brief, we modelled the measured fMRI signal as

$$y(t) = p(t)\beta + e$$

where $p(t)$ is the predicted BOLD signal in each voxel at time t, β is a scaling coefficient that accounts for unknown units of the BOLD signal and e is the residual error. The predicted response $p(t)$ was calculated by modelling the receptive field of the neuronal population within each voxel using a two-dimensional Difference of Gaussians of the form

$$f(x,y) = e^{\frac{-(x-x0)^2+(y-yo)^2}{2\sigma_1^2}} - \delta e^{\frac{-(x-x0)^2+(y-yo)^2}{2\sigma_2^2}}$$

where σ_1 and σ_2 is the standard deviations of the two Gaussians and δ is a parameter that modulates the amplitude of the second negative Gaussian. This model was combined with a matrix representation of the stimulus intensity at (x,y) for all time points in the acquired volumes. The result was summed for each volume and then convolved with SPMs standard hemodynamic model, and finally scaled with β. We used Matlab's implementation of the Nelder-Mead method (fminsearch) to obtain the pRF model parameters that best fit the data by minimizing the sum of squared error between the observed and predicted response.

DC-component

The results of the pRF analysis yielded a σ_1, σ_2, δ, x- and y coordinate for each of the included voxels. To compute the values of $\sigma 1$, $\sigma 2$, and δ that would result in a DC-balanced filter, we used the observed σ_1 and δ values in a Nelder-Mead search algorithm that minimized the squared integral of the pRF parameters of individual voxels and allowed σ_2 to vary. Supporting Figure 1 shows the result of this calculation for both hemispheres from two participants. There is a clear tendency towards agreement between the observed and the computed data, albeit with some additional noise.

For both the observed and the computed pRF parameters, we calculated their bandpass parameters by first transforming the data into a 2D discrete Fourier space and since the DoG is circularly symmetric in Fourier space, we used Matlabs findpeaks function to find the signal maximum (amplitude) on the centremost 1D representation of the absolute signal. From this peak we observed the corresponding peak frequency and calculated the full-width at half its maximum. Note that for the DoG in the spatial domain, the half maximum is defined as the point that falls half the distance between the DoG minimum and maximum. This is because this is the only case where the filter falls below zero (see Figure 3).

Small differences between the observed and computed σ and δ parameters have a rather large impact on the bandpass parameters – especially the bandwidth. The main reason for this is shown in Supporting Figure 2, and is connected to the way we compute the bandpass parameters; when a DC-bias is introduced in the bandpass filter, this may easily lead to a situation where the filter does not fall below the half-maximum point in the FWHM calculation and therefore the bandwidth is overestimated as exemplified in Supporting Figure 2B. An underestimation of the bandwidth is also seen when a strong DC-component is observed at the lowest frequencies as in Supporting Figure 2A and C.

To increase the signal to noise ratio, we pooled the data into eccentricity bins. Since pRF size is known to be relatively stable across polar angle for a given eccentricity in pRF experiments (Dumoulin & Wandell, 2008), we created 17 eccentricity bins of 1 degree visual angle each (from 0.5 to 17.5) and removed voxels with model fits that did not, at least, explain 5% of the BOLD signal variance. By inspecting plots of the individual DoG model parameter distribution, it was observed that they were not all normally distributed, so in these cases we used the median value within bins. In 741 out of 748 (22 participants x 2 hemispheres x 17 eccentricity bins), this procedure lead to non-zero parameter estimates, and these data points were used in further analysis.

Statistical analysis

Observed parameter values were log-transformed and normality was inspected using histograms and qq-plots. Data appeared normally distributed, apart from a small fraction of data points showing very large deviations (22 of 741, less than 3%, typically for the peak frequency parameter) indicative of poor pRF model fits. These were rejected before statistical modelling. Data were analysed in a random coefficient model with (log-transformed) observed parameter value as the dependent variable, (log-transformed) simulated parameter value as a covariate and random intercepts and slopes varying with Participant and Hemisphere within Participant. Whenever possible, residual error correlations were allowed to decrease exponentially with increasing difference in Eccentricity (for peak frequency, this model did not converge, and to ensure convergence, no assumptions was made for residual error correlations). Model fits were made using restricted maximum likelihood function with the Broyden-Fletcher-Goldfarb-Shanno (BFGS) algorithm.

Acknowledgements. This article is based upon work from COST Action CA18106, supported by COST (European Cooperation in Science and Technology). We thank D. S. Schwarzkopf for providing software for the pRF mapping as well as assistance in its usage. We thank A. G. Kristensen and M. B. Sørensen for assistance in data collection.

Competing interests. The authors declare no competing interests.

References

Albright, T. D., & Stoner, G. R. (2002). Contextual Influences on Visual Processing. *Annual Review of Neuroscience*, *25*, 339–379. https://doi.org/10.1146/annurev.neuro.25.112701.142900

Allman, J., Miezin, F., & McGuinness, E. (1985). Stimulus Specific Responses from Beyond the Classical Receptive Field: Neurophysiological Mechanisms for Local-Global Comparisons in Visual Neurons. *Annual Review of Neuroscience*, *8*, 407–430.

Barlow, H. B. (1961). Possible Principles Underlying the Transformations of Sensory Messages. *Sensory Communication*, 216–234. https://doi.org/10.7551/mitpress/9780262518420.003.0013

Bijanzadeh, M., Nurminen, L., Merlin, S., Clark, A. M., & Angelucci, A. (2018). Distinct Laminar Processing of Local and Global Context in Primate Primary Visual Cortex. *Neuron*, *100*(1), 259-274.e4. https://doi.org/10.1016/j.neuron.2018.08.020

Blakemore, C., & Tobin, E. A. (1972). Lateral inhibition between orientation detectors in the cat's visual cortex. *Experimental Brain Research*, *15*(4), 439–440. https://doi.org/10.1007/BF00234129

Brainard, D. H. (1997). The Psychophysics Toolbox. *Spatial Vision*, *10*(4), 433–436. https://doi.org/10.1163/156856897X00357

Cavanaugh, J. R., Bair, W., & Movshon, J. A. (2002). Nature and Interaction of Signals From the Receptive Field Center and Surround in Macaque V1 Neurons. *Journal of Neurophysiology*, *88*(5), 2530–2546. https://doi.org/10.1152/jn.00692.2001

Dalal, N., & Triggs, B. (2005). Histograms of oriented gradients for human detection. *Proceedings - 2005 IEEE Computer Society Conference on Computer Vision and Pattern Recognition, CVPR 2005*. https://doi.org/10.1109/CVPR.2005.177

Dale, A. M., Fischl, B., & Sereno, M. I. (1999). Cortical surface-based analysis. I. Segmentation and surface reconstruction. *NeuroImage*, *9*(2), 179–194. https://doi.org/10.1006/nimg.1998.0395

Daugman, J. G. (1985). Uncertainty relation for resolution in space, spatial frequency, and orientation optimized by two-dimensional visual cortical filters. *Journal of the Optical Society of America A*, *2*(7), 1160–1169. https://doi.org/10.1364/josaa.2.001160

den Bergh, G. Van, Zhang, B., Arckens, L., & Chino, Y. M. (2010). Receptive-field properties of V1 and V2 neurons in mice and macaque monkeys. *The Journal of Comparative Neurology*, *518*(11), 2051–2070. https://doi.org/10.1002/cne.22321

Dumoulin, S. O., & Wandell, B. a. (2008). Population receptive field estimates in human visual cortex. *NeuroImage*, *39*(2), 647–660. https://doi.org/10.1016/j.neuroimage.2007.09.034

Field, D. J. (1987). Relations between the statistics of natural images and the response properties of cortical cells. *Journal of the Optical Society of America A*, *4*(12), 2379. https://doi.org/10.1364/JOSAA.4.002379

Fischl, B., Sereno, M. I., & Dale, A. M. (1999). Cortical surface-based analysis. II: Inflation, flattening, and a surface-based coordinate system. *NeuroImage*, *9*(2), 195–207. https://doi.org/10.1006/nimg.1998.0396

Gabor, D. (1946). Theory of Communication. *Journal of the Institution of Electrical Engineers - Part III: Radio and Communication Engineering*, *93*(26), 429–441.

Gonzalez, R., & Woods, R. (2002). Digital image processing. In *Prentice Hall*. https://doi.org/10.1016/0734-189X(90)90171-Q

Hartline, H. K., Wagner, H. G., & Ratliff, F. (1956). Inhibition in the eye of Limulus. *The Journal of General Physiology*, *39*(5), 651–673. https://doi.org/10.1085/jgp.200709918

Harvey, B. M., & Dumoulin, S. O. (2012). Modeling center – surround configurations in population receptive fields using fMRI Wietske Zuiderbaan. *Journal of Vision*, *12*(3), 1–15. https://doi.org/10.1167/12.3.10.Introduction

Heisenberg, W. (1927). The actual content of quantum theoretical kinematics and mechanics. *Zeitschrift Für Physik*. https://doi.org/10.1119/1.1991172

Hinds, O. P., Rajendran, N., Polimeni, J. R., Augustinack, J. C., Wiggins, G., Wald, L. L., … Fischl, B. (2008). Accurate prediction of V1 location from cortical folds in a surface coordinate system. *NeuroImage*. https://doi.org/10.1016/j.neuroimage.2007.10.033

Hyvärinen, A., Hurri, J., & Hoyer, P. O. (2009). Natural Image Statistics-A Probabilistic Approach to Early Computational Vision. In *Computational Imaging and Vision*.

Kennard, E. H. (1927). Zur Quantenmechanik einfacher Bewegungstypen. *Zeitschrift Für Physik*. https://doi.org/10.1007/BF01391200

Kok, P., Bains, L. J., Van Mourik, T., Norris, D. G., & De Lange, F. P. (2016). Selective activation of the deep layers of the human primary visual cortex by top-down feedback. *Current Biology*, *26*(3), 371–376. https://doi.org/10.1016/j.cub.2015.12.038

Kovesi, P. (2010). Fast almost-Gaussian filtering. *Proceedings - 2010 Digital Image Computing: Techniques and Applications, DICTA 2010*, 121–125. https://doi.org/10.1109/DICTA.2010.30

Lindeberg, T. (2013). A computational theory of visual receptive fields. *Biological Cybernetics*, *107*(6), 589–635. https://doi.org/10.1007/s00422-013-0569-z

Marr, D., & Hildreth, E. (1980). Theory of edge detection. *Proceedings of the Royal Society of London. Series B, Containing Papers of a Biological Character. Royal Society (Great Britain)*, *207*(1167), 187–217. https://doi.org/10.1098/rspb.1980.0020

Nelson, J. I., & Frost, B. J. (1978). Orientation-selective inhibition from beyond the classic visual receptive field. *Brain Research*, *139*(2), 359–365. https://doi.org/10.1016/0006-8993(78)90937-X

Nurminen, L., & Angelucci, A. (2014). Multiple components of surround modulation in primary visual cortex: Multiple neural circuits with multiple functions? *Vision Research*, *104*, 47–56. https://doi.org/10.1016/j.visres.2014.08.018

Olsen, S. R., & Wilson, R. I. (2008). Lateral presynaptic inhibition mediates gain control in an olfactory circuit. *Nature*, *452*, 956–960. https://doi.org/10.1038/nature06864

Pelli, D. G. (1997). The VideoToolbox software for visual psychophysics: transforming numbers into movies. *Spatial Vision*, *10*(4), 437–442. https://doi.org/10.1163/156856897X00366

Rodieck, R. W. (1965). Quantitative analysis of cat retinal ganglion cell response to visual stimuli. *Vision Research*, *5*(12), 583–601. https://doi.org/10.1016/0042-6989(65)90033-7

Sachdev, R. N. S., Krause, M. R., & Mazer, J. A. (2012). Surround suppression and sparse coding in visual and barrel cortices. *Frontiers in Neural Circuits*, *6*(43). https://doi.org/10.3389/fncir.2012.00043

Sceniak, M. P., Hawken, M. J., & Shapley, R. (2001). Visual spatial characterization of macaque V1 neurons. *Journal of Neurophysiology*, *85*(5), 1873–1887.

Schwarzkopf, D. S., Anderson, E. J., de Haas, B., White, S. J., & Rees, G. (2014). Larger Extrastriate Population Receptive Fields in Autism Spectrum Disorders. *Journal of Neuroscience*, *34*(7), 2713–2724. https://doi.org/10.1523/JNEUROSCI.4416-13.2014

Sereno, M. I., Dale, A. M., Reppas, J. B., Kwong, K. K., Belliveau, J. W., Brady, T. J., … Tootell, R. B. H. (1995). Borders of Multiple Visual Areas In Humans Revealed By Functional MRI. *Science*, *268*, 889–893.

Shushruth, S., Ichida, J. M., Levitt, J. B., & Angelucci, A. (2009). Comparison of Spatial Summation Properties of Neurons in Macaque V1 and V2. *Journal of Neurophysiology*, *102*(4), 2069–2083. https://doi.org/10.1152/jn.00512.2009

Shushruth, S., Mangapathy, P., Ichida, J. M., Bressloff, P. C., Schwabe, L., & Angelucci, A. (2012). Strong Recurrent Networks Compute the Orientation Tuning of Surround Modulation in the Primate Primary Visual Cortex. *Journal of Neuroscience*, *32*(1), 308–321. https://doi.org/10.1523/JNEUROSCI.3789-11.2012

Slllito, A. M., Grieve, K. L., Jones, H. E., Cudeiro, J., & Davls, J. (1995). Visual cortical mechanisms detecting focal orientation discontinuities. *Nature*, *378*, 492–496. https://doi.org/10.1038/378492a0

Stork, D. G., & Wilson, H. R. (1990). Do Gabor functions provide appropriate descriptions of visual cortical receptive fields? *J Opt Soc Am A*.

Sutter, M. L., Schreiner, C. E., McLean, M., O'Connor, K. N., & Loftus, W. C. (1999). Organization of inhibitory frequency receptive fields in cat primary auditory cortex. *Journal of Neurophysiology*, *82*(5), 2358–2371. https://doi.org/10.1152/jn.1999.82.5.2358

Vega, B. F., & Johnson, K. O. (1999). Surround suppression in the responses of primate SA1 and RA mechanoreceptive afferents mapped with a probe array. *J Neurophysiol*, *81*(6), 2177–2719.

Zuiderbaan, W., Harvey, B. M., & Dumoulin, S. O. (2012). Modeling center – surround configurations in population receptive fields using fMRI. *Journal of Vision*, *12*(3), 1–15. https://doi.org/10.1167/12.3.10.Introduction